PNAS RESEARCH ARTICLE | APPLIED PHYSICAL SCIENCES

Assessing continuum plasticity postulates with grain stress and local strain measurements in triaxially compressed sand

Ryan C. Hurley[a,b,1], Ghassan Shahin[b,c], Brett S. Kuwik[a], and Kwangmin Lee[a]

Edited by David Weitz, Harvard University, Cambridge, MA; received January 29, 2023; accepted June 30, 2023

Critical state and continuum plasticity theories have been used in research and engineering practice in soil and rock mechanics for decades. These theories rely on postulated relationships between material stresses and strains. Some classical postulates include coaxiality between stress and strain rates, stress–dilatancy relationships, and kinematic assumptions in shear bands. Although numerical and experimental data have quantified the strains and grain kinematics in such experiments, little data quantifying grain stresses are available. Here, we report the first-known grain stress and local strain measurements in triaxial compression tests on synthetic quartz sands using synchrotron X-ray tomography and 3D X-ray diffraction. We use these data to examine the micromechanics of shear banding, with a focus on coaxiality, stress-dilatancy, and kinematics within bands. Our results indicate the following: 1) elevated deviatoric stress, strain, and stress ratios in shear bands throughout experiments; 2) coaxial principal compressive stresses and strains throughout samples; 3) significant contraction along shear bands; 4) vanishing volumetric strain but nonvanishing stress fluctuations throughout samples at all stages of deformation. Our results provide some of the first-known in situ stress and strain measurements able to aid in critically evaluating postulates employed in continuum plasticity and strain localization theories for sands.

granular materials | continuum plasticity | X-ray imaging | triaxial tests | shear bands

Critical state and continuum plasticity theories are an essential component of research and engineering practice in soil mechanics and rock mechanics (1, 2). Such theories posit the existence of a steady-state of material deformation after shearing to very large strains (1–3). At this steady state, or critical state, a sheared granular material or rock maintains a constant volume and void ratio, hydrostatic pressure, and deviatoric stress (4, 5). Contemporary extensions of critical state theory for sands also posit that fabric (e.g., contact or particle orientations) and particle size become constant at critical state (5–9). The precise strain at which critical state is reached has been the subject of extensive investigation (4, 6, 8, 9) and depends on whether the definition of critical state includes consideration of fabric and breakage, which may require significantly larger shear strains to reach a constant value than do stresses and strains.

Triaxial compression tests are some of the most common tests used to quantify the mechanical behavior of geomaterials in the context of critical state and continuum plasticity theories (1, 2, 10). Triaxial tests, as well as biaxial and shear tests, can be analyzed at a macroscopic level to quantify a material's evolving stiffness, yield strength, and critical state strength. Triaxial tests have corroborated the conventional understanding of volumetric strain and shear stress evolution before and after critical state in a broad variety of soils and rocks (2, 6, 9, 11). These tests have also revealed the ubiquitous emergence of shear bands, or regions of localized shear strain which become fully developed when a material approaches a macroscopic critical state. The emergence of shear bands may be accompanied by dilation at low pressures, compaction at high pressures, or may feature a more complex volumetric evolution depending on a soil's initial density, breakage susceptibility, and the confining pressure applied to the sample (2, 12–15).

There is significant evidence that unconsolidated sands and sediments and poorly lithified sandstones undergo shear banding, accompanied by either dilation at low pressures or compaction at high pressures, throughout the Earth's upper crust (16–19). The mechanical behavior of these materials, and specifically their propensity to develop shear and deformation bands, is of significant importance because of their application as reservoirs for hydrocarbon extraction and CO_2 storage (20). These materials have therefore been tested under conditions similar to those found in their reservoir applications (5 to 50 MPa) (13, 19–22), and their mechanical behaviors have been interpreted using critical state plasticity theories (16–18).

Significance

Plasticity theories have been used for decades in research and engineering practice to predict the mechanical behavior of sands, soils, powders, and rocks. These theories rely upon postulated relationships between stresses and strain rates in different regions of a material before and after plastic flow. Measuring such stresses has been a significant experimental challenge. Here, we employ X-ray imaging and diffraction to measure internal stresses and strains in triaxially compressed sands. Our results provide some of the first data able to assess postulated relationships between stress and strain within samples during and after plastic flow, with implications for validating and extending constitutive models used throughout soil and rock mechanics.

Author affiliations: [a]Department of Mechanical Engineering, Johns Hopkins University, Baltimore, MD 21218; [b]Hopkins Extreme Materials Institute, Johns Hopkins University, Baltimore, MD 21218; and [c]Laboratory of Experimental Rock Mechanics, School of Architecture, Civil and Environmental Engineering, Civil Engineering Institute, École Polytechnique Fédérale de Lausanne, Lausanne 1015, Switzerland

Author contributions: R.C.H. and G.S. designed research; R.C.H., B.S.K., and K.L. performed research; R.C.H. analyzed data; and R.C.H. wrote the paper.

The authors declare no competing interest.

This article is a PNAS Direct Submission.

Copyright © 2023 the Author(s). Published by PNAS. This article is distributed under Creative Commons Attribution-NonCommercial-NoDerivatives License 4.0 (CC BY-NC-ND).

[1]To whom correspondence may be addressed. Email: rhurley6@jhu.edu.

This article contains supporting information online at https://www.pnas.org/lookup/suppl/doi:10.1073/pnas.2301607120/-/DCSupplemental.

Published July 31, 2023.

Downloaded from https://www.pnas.org by "JOHN HOPKINS UNIVERSITY, MT WASHINGTON SHERIDAN LIB TECH SERVICES" on August 9, 2023 from IP address 162.129.251.86.

From a theoretical perspective, shear bands emerging in triaxial tests and other test configurations have classically been interpreted as instabilities in macroscopic constitutive relations, or as bifurcations (23–26). To formulate constitutive laws, classical assumptions regarding internal stresses and strains in triaxial tests have been made. A nonexhaustive list of these assumptions includes the following: coaxiality of stress and strain rates in shear zones (1, 27, 28); zero extension along shear bands (29); existence of stress–dilatancy relationships and vanishing dilatancy at critical state (30–32); associative or nonassociative plastic flow (1); and the formation of "dead zones" outside of shear bands at critical state (33). Direct experimental evidence to support or contradict these assumptions has typically only been available for assumptions regarding strains and strain heterogeneity because of challenges in experimentally measuring stresses in and out of shear bands.

To examine strain localization and the preceding assumptions experimentally, prior research has employed photoelasticity in biaxial compression experiments (27, 34, 35), X-ray radiography (29), acoustic emissions measurements (20), and high-resolution X-ray computed tomography (XRCT) in triaxial tests (13, 36–38). These studies have offered evidence supporting the assumptions of coaxiality in 2D granular packings (27, 34, 35) and zero extension and vanishing dilation at critical state in shear bands in sands (29, 39). Recent experiments using XRCT have revealed rich particle scale kinematics in shear bands, including rotations, breakage, and force chain structures (12, 13, 36–38, 40–44), which are not considered in conventional plasticity theories but are incorporated into some modern constitutive frameworks such as continuum breakage mechanics (45, 46). Detailed discrete element method (DEM) simulations, recently applied to "digital twins" or direct replicas of physical specimens, have also quantified force chains and principal stress rotations in shear bands (47–49). Recent experiments employing XRCT, and accompanying numerical simulations, have also advanced a variety of methods for identifying shear bands based on grain rotations, relative displacements, angular velocity, particle contact (or coordination) numbers, and local void ratios (50–54). Furthermore, recent theoretical and numerical studies have highlighted the importance of the distinct mechanical responses (stresses, strains, and length scales) in and out of shear bands and have begun to incorporate shear band features into constitutive frameworks such as the double-scale approach (55–57).

While strain heterogeneity has been extensively characterized in and out of shear bands within triaxial tests, there has been relatively little in situ measurement of grain stresses, particularly in 3D. Recent work employing XRCT along with 3D X-ray diffraction (3DXRD) in experiments on sands and synthetic soils has yielded some of the first insight into grain stresses, local strains, and a variety of related properties (50, 58–61). However, such experiments have not yet been performed in carefully controlled triaxial compression settings to address the assumptions noted in this introduction.

The primary objective of this paper is to quantitatively investigate grain stresses and their relationship to local strains and kinematics in triaxially compressed sand samples. To achieve this, we use in situ synchrotron XRCT and 3DXRD to study synthetic sand in a miniature triaxial compression instrument. The use of this approach, the only known approach through which grain stresses can be measured experimentally, necessitates using of higher confining pressures and smaller samples than are typically used in experimental studies of dilatant shear bands performed in the soil mechanics communities. Our triaxial tests therefore feature compactive, rather than dilative, shear bands, which emerge naturally in many geomaterials deformed under relatively high confining pressures (2, 12, 13). Experimental constraints also required the use of less than 2,000 particles per sample, suggesting the possibility of finite size and boundary effects. However, boundary and size effects in triaxial tests are still the subject of study and debate in geomechanics (62–66), and we are careful to offer explanations for differences between the responses of the small samples used here and larger samples found in the literature. Despite the limitations of our experiments, the data and analysis serve a critical need for numerical and theoretical researchers developing constitutive models and studying the critical state behavior of soils and rocks.

Our major results indicate that deviatoric stresses and strains, stress ratios, and grain rotations are significantly elevated within shear bands; principal compressive stresses and strain rates are coaxial in and out of bands; bands feature significant contraction along their shearing direction; dilatancy tends to zero everywhere at critical state; plastic work remains elevated in bands and is small but nonnegligible outside of bands; and grain stress fluctuations in and out of bands reach a similar magnitude long before steady-state flow and suggest continued stress redistribution in and out of bands at critical state. These findings offer new data to corroborate the fundamental concept that triaxial tests are not elemental and should be interpreted by considering the distinct behaviors which occur in and out of shear bands. The findings motivate revisiting recent and classical theoretical and experimental work investigating distinct behaviors in and out of shear bands (55, 57), coaxiality of stresses and strain rates (27), stress–dilatancy relationships (30, 32), and plastic work and stress fluctuations in and out of bands (33, 56).

Results and Discussion

Experiments. We performed triaxial compression tests on synthetic quartz sand using a recently developed triaxial compression instrument capable of subjecting sand samples to 50 MPa confining pressure while axially straining them (67) (Fig. 1*A*). Full details on sand preparation, mechanical testing, and data acquisition protocols are given in *Materials and Methods*. Dry, well-rounded sand with a mean equivalent diameter of 140 μm was poured into membranes placed on the mechanical compression platens of the triaxial compression instrument. Membranes were externally sealed with a cap and vacuum grease to prevent fluid saturation before tests were performed. Tests were performed at 20, 30, and 35 MPa applied confining pressure, p_c, at the Advanced Photon Source (APS) beamtime ID-1. Elevated confining pressures were used to ensure that grain strains were measurable via 3DXRD, which has a strain resolution of 10^{-4} for on-diagonal and 5×10^{-5} for off-diagonal strain tensor components (68, 69), and therefore necessitates elevated sample stresses to induce measurable strains within grains. Sample sizes were also limited by the 1.5 × 1.5 mm X-ray beam size and the 144-h continuous experiment time limit at ID-1, during which all equipment and sample setup, detector calibration, and measurements must be performed. 3DXRD and XRCT measurements were made in situ during fixed axial sample strain at each of the symbols in Fig. 1*D*. Diffraction spots generated from synthetic quartz (SiO_2) were analyzed in MIDAS (Fig. 1*B*), providing grain strain tensors (with 1×10^{-4} on-diagonal and 5×10^{-5} off-diagonal resolution), orientations (within 0.05°), and positions (within a few microns) for between 55% and 85% of grains (see *Materials and Methods* and

Downloaded from https://www.pnas.org by "JOHN HOPKINS UNIVERSITY, MT WASHINGTON SHERIDAN LIB TECH SERVICES" on August 9, 2023 from IP address 162.129.251.86.

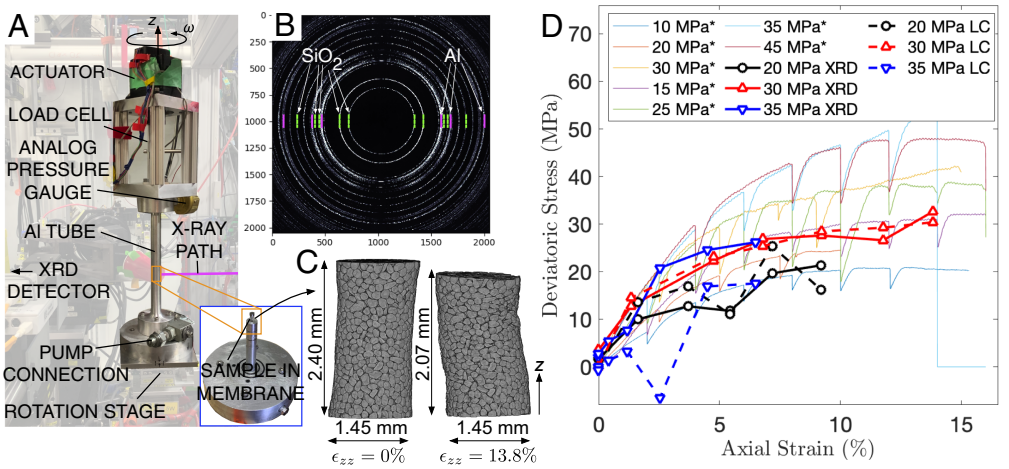

Fig. 1. Experimental setup and macroscopic sample response. (*A*) Experimental apparatus employed in triaxial compression tests, showing major components including an aluminum (Al) tube in which synthetic sand samples were located within membranes, the X-ray path, and the actuator for generating axial compression in the *z*-direction. More details can be found in ref. 67. (*B*) Diffraction patterns obtained on the flat panel XRD detector used for 3DXRD diffraction analysis (*Materials and Methods*). (*C*) Segmented XRCT images obtained for the sample subjected to 30 MPa confining pressure. Samples are kept in or near the X-ray path throughout experiments, as indicated by the figure. (*D*) Deviatoric stress versus axial sample strain for the three samples tested. Curves with both lines and symbols represent the responses of samples tested for this paper, with symbols indicating the stress and strain state at which XRCT and 3DXRD measurements were made. Pressure labels are target pump pressures, not actual homogenized pressures as described in main text. Curves labeled XRD indicate stresses measured through 3DXRD at the corresponding sample axial strain for the corresponding nominal confining pressure. Curves labeled LC indicate stresses measured using the load cell (*Materials and Methods*). Other curves marked with an asterisk (*) are data from recent work with the same triaxial apparatus (13). Those data are from tests involving either about 10,000 Ottawa sand grains with a D_{50} of 300 μm (10, 20, and 30 MPa) or from tests involving about 30,000 Ottawa sand grains with a D_{50} of 175 μm (15, 25, 35, and 45 MPa).

SI Appendix). Using the known elastic constants and orientations of each SiO_2 crystal, Hooke's law was used to calculate stress tensors for each grain (with 12 MPa on-diagonal and 6 MPa off-diagonal resolution). Errors in individual grain strain and stress tensor measurements are known to be normally distributed with SDs approximately equal to the resolutions noted above (68, 69). Measured grain strains and calculated stresses are therefore as likely to be higher as they are to be lower than their true values. Volume-averaged, also referred to as homogenized, stresses reported in this paper for entire samples or regions containing a significant number of grains are therefore expected to feature minimal systematic bias by the central limit theorem (70).

XRCT images were generated from radiographs using TomoPy (71) and analyzed in Matlab and the Python Software for Practical Analysis of Materials (SPAM) (72). Analysis of XRCT data yielded segmented 3D images with each particle identified by unique pixels (Fig. 1*C*), interparticle contact positions and orientations, grain displacements and rotations from digital volume correlation (DVC), and local strains between strain increments (*Materials and Methods*).

Mechanical testing involved subjecting samples to the confining pressures and axial strains shown in Fig. 1*D* while measuring deviatoric stresses using 3DXRD (labeled XRD) and the load cell (labeled LC). Although confining pressures, p_c, of 20, 30, and 35 MPa were imposed on samples, actual average mean stresses felt by the sample, as obtained by 3DXRD measurements, fluctuated between 10 and 30 MPa (Fig. 5). The stiffness of the membrane surrounding samples alone cannot fully explain this discrepancy between imposed and observed pressures (see discussion and other explanations, such as nonuniform chamber pressure, in *SI Appendix*). Nevertheless, maximum deviatoric stresses generally increased with confining pressure and reached a steady state after approximately 5 to 8% axial sample strain. Despite containing only between 1,600 and 1,900 grains, deviatoric stress versus strain followed trends very similar to samples containing over 30,000 Ottawa sand grains (13), shown as thin curves in Fig. 1*D*. Deviations of the response of samples studied here from larger samples described elsewhere (13) likely reflect finite size effects. The samples labeled as 30 and 35 MPa in Fig. 1*D* for this study follow similar trends because actual mean pressures measured by 3DXRD were approximately 20 MPa in both cases (see Fig. 5 and associated discussion).

Local Strain and Shear Band Identification. Local strains around grains were obtained between each increment of sample strain for each test using methods in refs. 59 and 73. These local strains are measured at the scale of the Voronoi cells surrounding each grain after the generation of a Voronoi tessellation, as described in *Materials and Methods*. Prior work has used a combination of grain rotations, relative displacements, angular velocity, coordination numbers, and local void ratios to identify shear bands (38, 50–54). Here, we identified shear bands using local deviatoric strains, ϵ_{dev}, consistent with recent work (47) and confirmed to identify similar regions, albeit in dilative shear bands, to those obtained based on enhanced grain rotations, angular velocities, reduced coordination numbers, and reduced void ratios (53). We first fit a plane to the positions of grains with local ϵ_{dev} greater than 1.5 times the mean ϵ_{dev}. We then consider grains with centers of mass within $\pm 1.5\ D_{50}$ (the mean grain diameter), or ±210 μm, of the plane to be part of shear bands. This width is consistent with the observed width of regions featuring ϵ_{dev} strains greater than 1.5 times the mean ϵ_{dev} for most axial sample strains for all samples (see *SI Appendix* for a rendering of particle positions used to identify shear bands). The width of our shear bands is slightly smaller than the width of shear bands between 6 and 7 D_{50} identified in well-rounded Caicos Ooids in (38). This reduced shear band width likely results in part from the small sample sizes used in this study but may also stem from the elevated confining pressures which have been linked to decreasing shear band widths (28, 74). Although shear bands are understood to change width as they develop (12, 47, 75), we keep this width constant in our analysis for convenience.

Downloaded from https://www.pnas.org by "JOHN HOPKINS UNIVERSITY, MT WASHINGTON SHERIDAN LIB TECH SERVICES" on August 9, 2023 from IP address 162.129.251.86.

Fig. 2 *A*, *D*, and *G* show segmented XRCT images of each sample in their initial and final states (see *SI Appendix* for images of other states). Each final state features grains colored by the magnitude of grain rotation between the second-to-last and last load step of the corresponding experiment. Shear bands are identified with dashed lines. Enhanced grain rotations visible in shear bands featured up to twice the magnitude of rotations outside of bands, as quantified in Fig. 2 *C*, *F*, and *I*, consistent with findings of prior work (13, 38). Shear bands also featured clearly enhanced local deviatoric and axial strain increments as shown in Fig. 2 *A*, *D*, and *G* and quantified in Fig. 2 *B*, *E*, and *H*. Also shown in Fig. 2 *B*, *E*, and *H* are the incremental deviatoric and volumetric strains homogenized in, above, and below shear bands at each strain level for each sample. Incremental strains in each region were homogenized by averaging all local strains weighted by each grain's Voronoi volumes (*Materials and Methods*). Incremental deviatoric strains in shear bands reached more than twice the incremental shear strains outside of bands, which generally remained small but nonnegligible in all experiments. Incremental volumetric strains were much smaller than deviatoric strains both in and out of bands. For all samples, incremental volumetric strains were slightly contractive in bands and either contractive or slightly dilative outside of bands. Volumetric strains in and out of shear bands are revisited later in this paper in discussion of Fig. 6 and stress–dilatancy relations.

The incremental normal strain parallel and perpendicular to the steepest inclination of the shear band was assessed by calculating $\boldsymbol{t}_1 \cdot \delta\boldsymbol{\epsilon} \cdot \boldsymbol{t}_1$ and $\boldsymbol{t}_2 \cdot \delta\boldsymbol{\epsilon} \cdot \boldsymbol{t}_2$, respectively, where $\boldsymbol{t}_1$ ($\boldsymbol{t}_2$) is the direction parallel (perpendicular) to the inclination and shearing direction of the shear band shown in Fig. 2 *A*, *D*, and *G*, and $\delta\boldsymbol{\epsilon}$ is the homogenized incremental strain tensor in the shear band. These calculations were performed to evaluate Roscoe's assumption of zero extension along the shear band (29) required for his and others' formulations of strength relationships (32). As shown in Fig. 2 *B*, *E*, and *H*, the incremental normal strains parallel and perpendicular to the steepest inclination of the shear band featured significant contraction and dilation, respectively. The presence of both contraction and dilation in orthogonal directions implies that a direction of zero-extension exists within the plane of the band; however, it is not aligned with the shearing direction. Similar violations of this zero-extension hypothesis have been reported in prior studies which have identified strain fluctuations in well-developed shear bands (13, 41, 75). This finding suggests that Roscoe's assumption (29) may need to be revisited, although its violation may not have a significant influence on predictions of associated plasticity theories. More importantly, this finding motivates revisiting the zero-extension

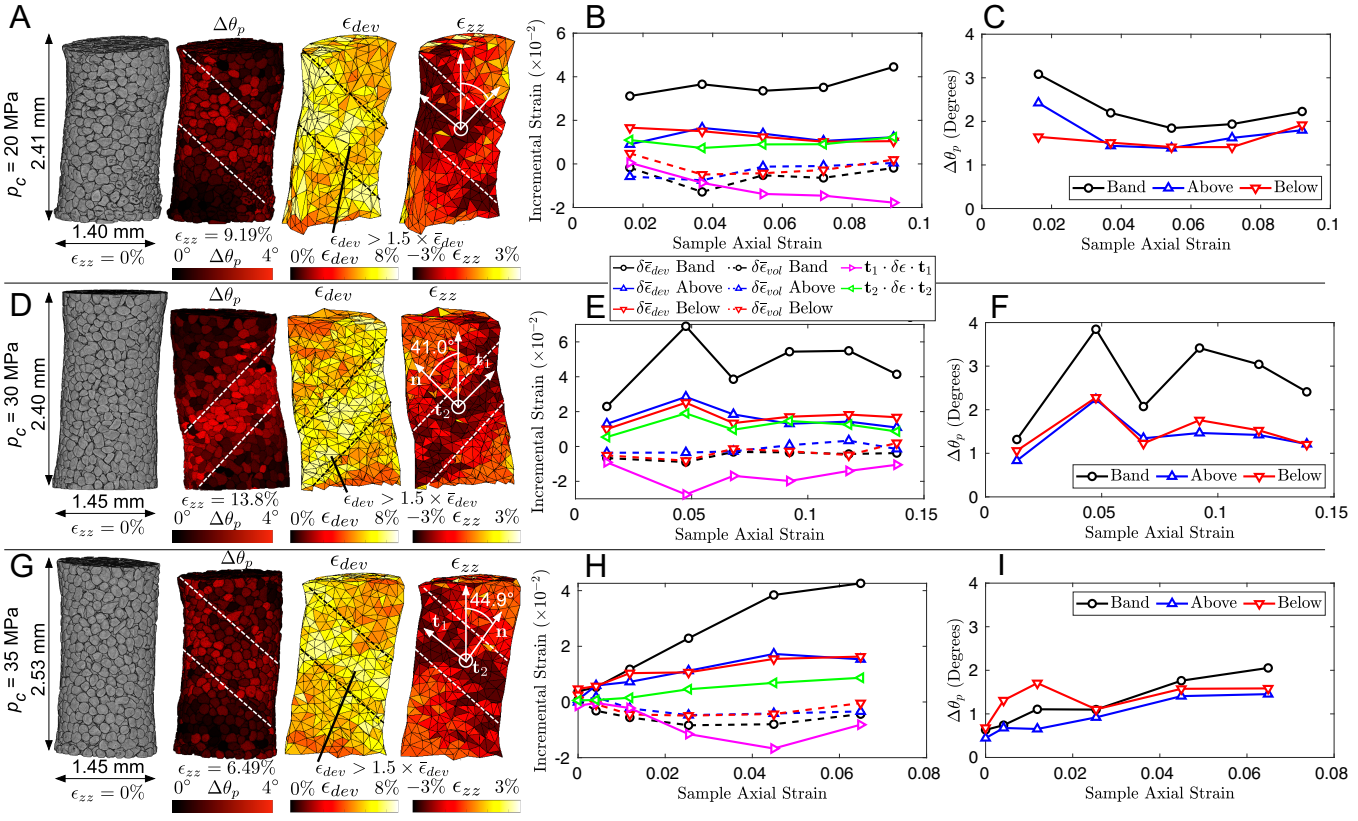

Fig. 2. Features of grain kinematics in and out of shear bands. *A* shows, for the sample subjected to 20 MPa confining pressure, from left to right: a rendering of the sample's initial state as portrayed in a segmented XRCT image; a rendering of the sample's final state with grains colored by the magnitude of grain rotation in degrees between the second-to-last and final strain increment; a rendering of incremental deviatoric tetrahedral strain in a vertical slice through the middle of the sample at the final strain increment; a rendering of incremental axial tetrahedral strain in a vertical slice through the middle of the sample at the final strain increment. For details on strain calculations, see *Materials and Methods*. Shear band inclination and the corresponding vectors $\boldsymbol{t}_1$ and $\boldsymbol{t}_2$ are explained in the main text. *B* shows, for the sample subjected to 20 MPa confining pressure, the homogenized incremental deviatoric and volumetric strain in, above, and below shear bands, as well as incremental strain normal and perpendicular to the direction of steepest shear band inclination at each strain increment. *C* shows, for the sample subjected to 20 MPa confining pressure, the average magnitude of grain rotation in degrees in, above, and below shear bands, as computed between the previous and current strain level. *D*, *E*, and *F* show the same information as *A*, *B*, and *C*, respectively, but for the sample subjected to 30 MPa confining pressure. *G*, *H*, and *I* show the same information as *A*, *B*, and *C*, respectively, but for the sample subjected to 35 MPa confining pressure.

Downloaded from https://www.pnas.org by "JOHN HOPKINS UNIVERSITY, MT WASHINGTON SHERIDAN LIB TECH SERVICES" on August 9, 2023 from IP address 162.129.251.86.

assumption in larger-scale laboratory triaxial tests and at lower confining pressures in which sands may be expected to undergo dilatant, rather than compactive, shear banding.

Shear Band Angles. The shear bands we identified using local ϵ_{dev} featured inclination angles shown in Fig. 3. Inclination angles and shear band locations identified with either strain measure were nearly identical after several percent axial strain of each sample. Each sample featured a shear band that approached a fairly constant inclination angle at maximum axial sample strain. Inclination angles were generally between 33° and 42° at maximum axial sample strain and increased with confining pressure, consistent with prior research (74).

Grain Stresses In and Out of Bands. Individual grain stress tensors were analyzed in and out of shear bands and were also homogenized in, above, and below bands. Homogenized stresses were calculated by multiplying an unweighted average of grain stresses by the solid fraction, $\boldsymbol{\sigma} = \phi_s(1/N_g)\sum_g^{N_g}\boldsymbol{\sigma}^g$, where ϕ_s is the solid fraction, N_g is the number of grains in a region, and $\boldsymbol{\sigma}^g$ is the grain stress tensor obtained from 3DXRD. This calculation of homogenized stress is akin to averaging methods in ref. 73 (see *Materials and Methods* for further details). The solid fraction ranged from 0.65 to 0.69 for each sample but was generally independent of sample strain (*SI Appendix*). Clearly enhanced porosity within shear bands, often observed in triaxial tests (39), was absent, because the confining pressures used in this study generated compactive, rather than dilative, shear bands (2, 13).

Individual grain stresses, σ_{zz}, and maximum principal compressive stresses, σ_1, are rendered for each sample at maximum strain in Fig. 4 *A*, *E*, and *I*. No clear patterns are evident in renderings of σ_{zz}. Renderings of σ_1 indicate general alignment of maximum principal compressive stresses with the sample's axial strain direction (the *z*-axis) and qualitatively suggest the presence of aligned chains of highly stressed particles reminiscent of force chains (58), although we do not explore identifying or studying these chains quantitatively here.

Homogenized deviatoric stresses and local deviatoric strains are first compared in, above, and below shear bands in Fig. 4 *B*, *F*, and *J*. Deviatoric stresses were computed by $q = \sqrt{3/2(\boldsymbol{s}:\boldsymbol{s})}$, where $\boldsymbol{s} = \boldsymbol{\sigma} - \mathrm{tr}(\boldsymbol{\sigma})\boldsymbol{I}/3$ is the deviatoric stress tensor, "tr" is the trace operator, $\boldsymbol{I}$ is the identity tensor, and ":" is a double contraction. Deviatoric stresses were anywhere from 3 to 8 MPa higher in shear bands than for the entire samples and up to 13 MPa higher than for regions outside of bands (e.g., Fig. 4*F*). This finding suggests that the macroscopic deviatoric stress measured in triaxial tests, labeled "Total" in Fig. 4 legends, may be significantly less than the maximum deviatoric stress experienced in shear bands, a finding not yet reported in the literature to the best of our knowledge. Related work examining stresses and strains in and out of bands from numerical data (55) suggest similar behaviors at moderate strains may be followed by a relaxation of deviatoric stresses when shear bands have undergone very large shear strains, as high as 50% or higher. Such strains were not possible in the present study due to the small sample sizes and the limited experimental duration.

Deviatoric strains in shear bands were about twice the total sample deviatoric strains at the end of each test. In contrast to (39), which found that void ratios evolved to a critical state more quickly in shear bands than outside of them, we did not find a more rapid approach to a final stress state in bands. Rather, we observed that it requires significantly more local strain in than out of shear bands to achieve a final stress state, consistent with other literature (55).

The deviatoric to mean stress ratio, q/p, was also found to be slightly higher in than out of shear bands at maximum axial sample strain (Fig. 4 *C*, *G*, and *K*). The mean stress was computed by $p = \mathrm{tr}(\boldsymbol{\sigma})/3$. This again suggests that the macroscopic q/p ratio measured in triaxial tests actually reflects a combination of a higher ratio inside and a lower ratio outside of shear bands, a result rarely reported in previous literature (76). The actual value of q/p at maximum sample strain was similar in samples subjected to 30 and 35 MPa confining pressures but increased to almost 2 for the sample subjected to 20 MPa confining pressure, likely because of significant reductions in confining pressure in the last load step of the 20 MPa experiment (see Fig. 5 and related discussion later in this paper).

A dashed line in Fig. 4 *C*, *G*, and *K* shows a stress–dilatancy relationship of the general form $\eta = M - \alpha D$, where $\eta = q/p$ at any axial sample strain, $M = q/p$ at critical state, taken as 1.2 for each sample, consistent with the ratio found at maximum axial strain for the samples subjected to 30 MPa and 35 MPa pressures, and at a sample strain of approximately 7% for the sample subjected to 20 MPa confining pressure. The quantity $D = -\delta\epsilon_{vol}/\delta\epsilon_{dev}$ is dilatancy (77), where subscripts *vol* and *dev* indicate volumetric and deviatoric incremental strain, respectively. Positive dilatancy indicates contraction while negative dilatancy indicates expansion.Incremental volumetric strain is computed by $\delta\epsilon_{vol} = \mathrm{tr}(\boldsymbol{\epsilon})$. Incremental deviatoric strain is computed analogously to deviatoric stress. We note that the proper definition of dilatancy requires the ratio to be calculated with plastic strains, rather than total strains, and thus, our value of D may be more appropriately referred to as an incremental deformation ratio. Nevertheless, we refer to it as dilatancy for simplicity. The dashed lines in Fig. 4 *C*, *G*, and *K* reasonably capture a portion of each sample's q/p evolution but break down at small or large axial sample strains.

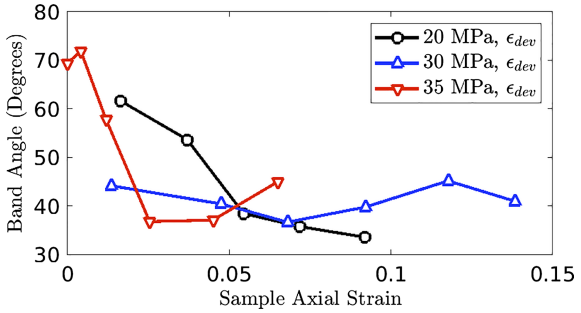

Fig. 3. Shear band inclination angle from the *z*-axis, determined as described in the main text using ϵ_{dev} in local regions around grains.

Stress and Strain Rate Orientations and Coaxiality. Maximum principal compressive stresses and strain rates were compared to assess the degree of their coaxiality, a common assumption of classical strength theories for soils and a frequently studied quantity in granular mechanics (1, 7, 27, 29, 31). In all samples, the angle between the maximum principal compressive stress and incremental strain (i.e., strain rate) was less than 10 degrees both in and out of shear bands at sample axial strains beyond 2%, as shown in Fig. 4 *D*, *H*, and *L*. Similarly, the principal compressive stress direction deviated less than 15 degrees from the vertical direction, the direction of macroscopic axial strain. The degree to which noncoaxiality of stress and strain rate and the rotation of principal stresses from globally imposed

Downloaded from https://www.pnas.org by "JOHN HOPKINS UNIVERSITY, MT WASHINGTON SHERIDAN LIB TECH SERVICES" on August 9, 2023 from IP address 162.129.251.86.

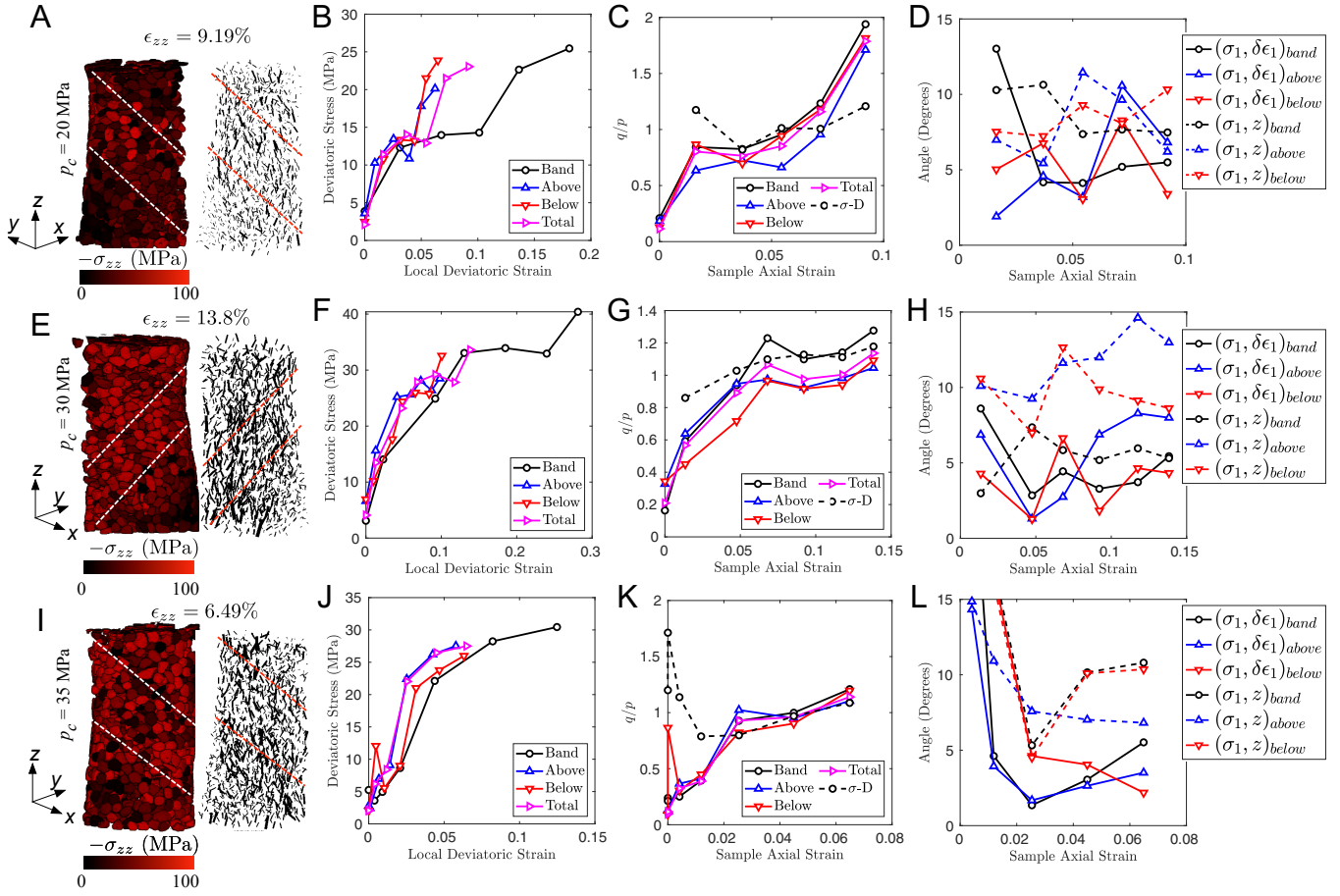

Fig. 4. Stress versus strain and strain rate coaxiality. *A* shows, for the sample subjected to 20 MPa confining pressure, a rendering of the sample at maximum sample strain with grains colored by stress tensor component σ_{ZZ} and a rendering of principal compressive stress directions and magnitudes, with lines scaled linearly in thickness and length by principal compressive stress magnitude. Only grains for which 3DXRD yielded stress measurements are rendered. *B* shows, for the sample subjected to 20 MPa confining pressure, the deviatoric stress versus local deviatoric strain for regions in, above, and below shear bands. *C* shows, for the sample subjected to 20 MPa confining pressure, the deviatoric to mean stress ratio, q/p, as a function of axial sample strain, as computed in, above, and below the shear bands, as well as for the entire sample. Dashed lines show the stress-dilatancy relationship, labeled $\sigma - D$, of the general form $\eta = M - \alpha D$, as described in the main text. *D* shows, for the sample subjected to 20 MPa confining pressure, the average angles, over particles in, above, and below shear bands, between the principal compressive stress direction (σ_1) and the principal compressive strain increment direction ($\delta\epsilon_1$) as well as between the between σ_1 and the *z*-axis. *E*, *F*, *G*, and *H* show the same information as *A*, *B*, *C*, and *D*, but for the sample subjected to 30 MPa confining pressure. *I*, *J*, *K*, and *L* show the same information as *A*, *B*, *C*, and *D*, but for the sample subjected to 35 MPa confining pressure.

strain directions would affect a theoretical prediction depends on the plasticity model being used (7, 29). While our finding of coaxiality is not surprising given that the well-rounded nature of the grains used in this study is not expected to induce the significant fabric anisotropy needed to sustain noncoaxiality (7), our observations confirm this coaxiality directly both in and out of shear bands for the first time in 3D. Furthermore, our finding that the principal compressive stresses are also well-aligned with the vertical direction in and out of shear bands is qualitatively consistent with recent work which has only been able to assess this alignment using numerical simulations (47).

Yield Locus and Flow Behavior. The deviatoric versus mean stress behavior of each sample is shown in Fig. 5. This figure confirms that the actual homogenized mean stresses experienced by samples fell below those imposed, thereby preventing the samples from experiencing the full magnitude of imposed pressure. See *Materials and Methods* and the *SI Appendix* for further discussion of possible sources for this discrepancy. Nevertheless, samples generally followed trends comparable to prior work (12, 13). Yield stress states indicated by right-pointing arrows are slightly higher than yield points identified in prior work, but here reflect the stress state at maximum sample strain rather than a perceived yielding points reported in prior work (13).

As identified previously in reference to Fig. 4, deviatoric and mean stresses within shear bands differ from those for each entire sample and for regions above and below bands. The drop in mean stress during the last strain increment for the sample subjected to 20 MPa confining pressure is responsible for the sudden increase in q/p in Fig. 4*C*. This drop likely occurred because of a minor leak in the Al pressure chamber surrounding the sample—the analog pressure gauge reading dropped approximately 1.4 MPa during the last load step for this sample, much less than the 5 MPa mean stress drop shown in Fig. 5 but still suggesting the possibility of a minor leak. The other samples did not experience a mean stress drop of a similar magnitude, and no change in analog pressure gauge reading occurred throughout experiments with those samples.

Dilatancy and Stress–Dilatancy Relationships. Many stress–dilatancy relationships exist in the literature and play fundamental roles in constitutive modeling of soils (32). Dilatancy values are shown in Fig. 6 *A*, *D*, and *G* for samples subjected to 20, 30, and 35 MPa, respectively. Dilatancy peaks at intermediate

Downloaded from https://www.pnas.org by "JOHN HOPKINS UNIVERSITY, MT WASHINGTON SHERIDAN LIB TECH SERVICES" on August 9, 2023 from IP address 162.129.251.86.

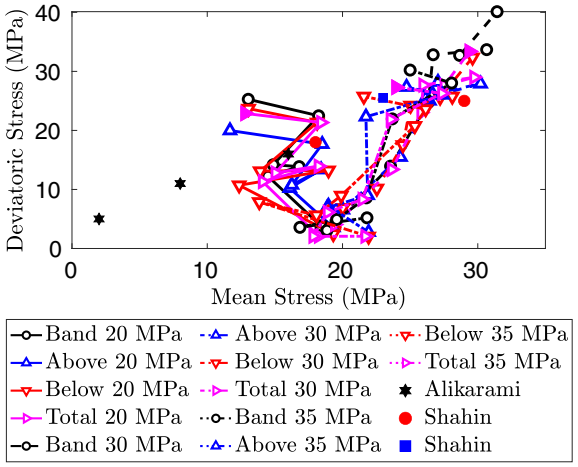

Fig. 5. Deviatoric versus mean stress paths for each sample based on homogenizing stresses in, above, and below shear bands, as well as throughout the entire sample. Solid right-pointing triangles represent the final stress state for homogenized stress throughout each entire sample. Pressure labels are target pump pressures, not actual homogenized pressures as described in main text. Alikarami refers to data from ref. 12. Shahin refers to data from ref. 13.

sample strains (for 20 and 35 MPa confining pressures) or early in the loading process (for 30 MPa confining pressure) but tends toward zero for all samples at large axial sample strains. For all samples, dilatancy at maximum axial sample strains suggests very small magnitudes of continued volumetric contraction within shear bands compensated by strain-neutral responses or minor volumetric expansion outside of bands. It is interesting to note that the total sample dilatancy in Fig. 6 *A*, *D*, and *G* (labeled "Total") closely mirrors the dilatancy in the shear band, while the off-band dilatancy often fluctuations in opposite senses above and below the dilatancy in the shear band. This may occur because of fluctuations in relative stiffness between the shear band and regions above and below the shear band, which would cause these regions to dilate or contract depending on their respective boundary conditions as shear progresses.

The basic stress–dilatancy relationship $\eta = M - \alpha D$, shown in Fig. 4 *C*, *G*, and *K* and explained in the related discussion, employs the dilatancy D calculated from the homogenized strains for each entire sample and an approximate stress ratio at yield (or near maximum strain), M, equal to 1.2. These basic stress–dilatancy relationships show a reasonable agreement with portions of the q/p curve for each sample. Deviations at large strains for the sample subjected to 20 MPa occur due to the large fluctuation in mean stress at the final strain increment. Deviations at small strains for the sample subjected to 35 MPa occur due to volumetric expansion and nearly strain-neutral sample responses at very small strains. Nevertheless, the stress–dilatancy relationships appear to qualitatively capture constitutive behavior over a moderate range of sample strains for each sample.

Work Rates. Work rates, $\boldsymbol{\sigma} \cdot \delta\boldsymbol{\epsilon}$, and especially plastic work rates, $\boldsymbol{\sigma} \cdot \delta\boldsymbol{\epsilon}^p$, where $\delta\boldsymbol{\epsilon}^p$ is the incremental plastic strain, are critical for constitutive modeling of soils and granular materials (e.g., ref. 78). Work rates are shown for each sample in Fig. 6 *B*, *E*, and

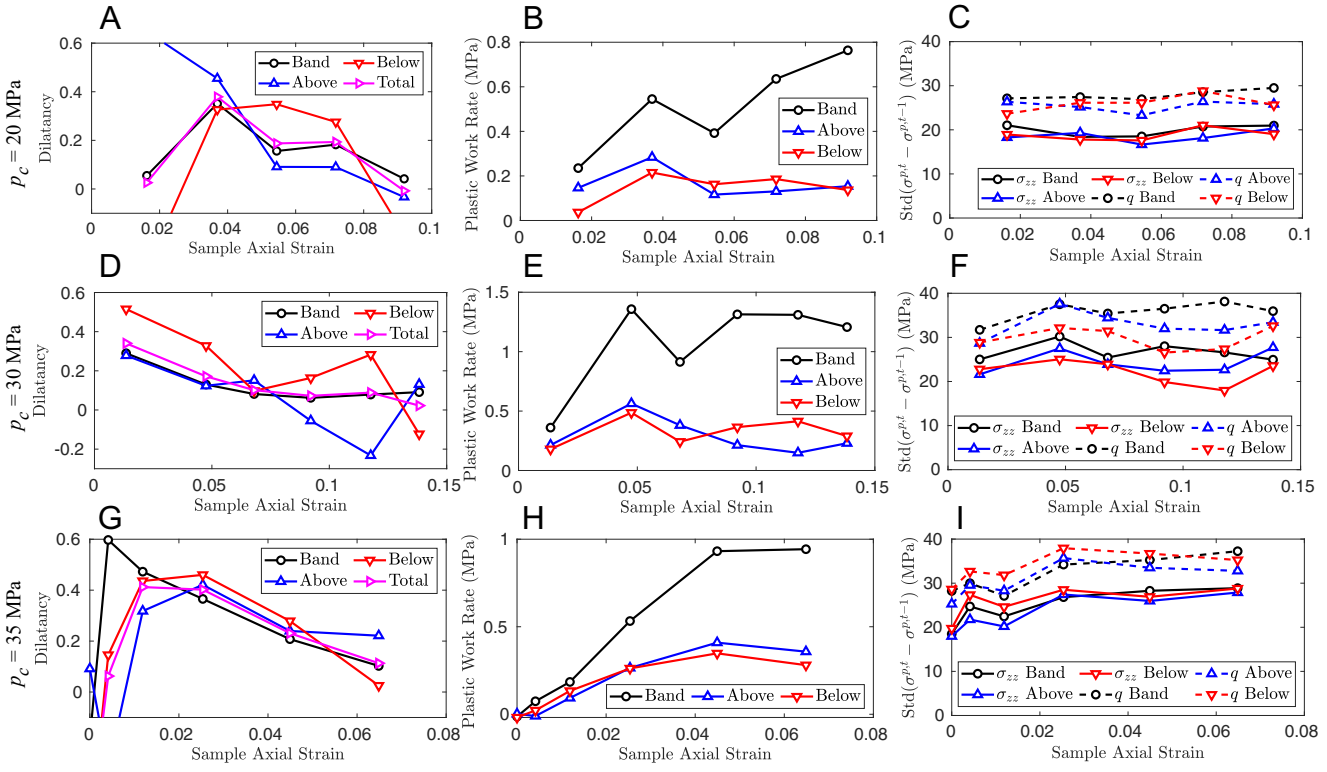

Fig. 6. Dilatancy, plastic work rates, and stress fluctuations. *A* shows, for the sample subjected to 20 MPa confining pressure, dilatancy, defined as $-\delta\epsilon_{vol}/\delta\epsilon_{dev}$, for grains in, above, and below bands, as well as for the entire sample. *B* shows, for the sample subjected to 20 MPa confining pressure, plastic work rates, defined as $\boldsymbol{\sigma} \cdot \delta\boldsymbol{\epsilon}$, in, above, and below shear bands. *C* shows, for the sample subjected to 20 MPa confining pressure, the average absolute value of per-grain stress fluctuations, defined as std($\sigma^{p,t} - \sigma^{p,t-1}$), where "std" is the SD, σ is σ_{zz} or q, t represents a load step, and $t-1$ represents the prior load step. These fluctuations are reported for all grains in, above, and below shear bands. *D*, *E*, and *F* show the same information as *A*, *B*, and *C*, but for the sample subjected to 30 MPa confining pressure. *G*, *H*, and *I* show the same information as *A*, *B*, and *C*, but for the sample subjected to 35 MPa confining pressure.

Downloaded from https://www.pnas.org by "JOHN HOPKINS UNIVERSITY, MT WASHINGTON SHERIDAN LIB TECH SERVICES" on August 9, 2023 from IP address 162.129.251.86.

H, under the assumption that all measured strain increments are plastic. Although this may be a strong assumption, our major conclusions below are unaffected by it. Work rates remain significantly elevated in shear bands at maximum axial sample strains at all pressure levels and are three to five times higher within bands than in regions above or below bands. Adopting a simple form of Taylor's work equation (79), $\phi = p\delta\epsilon_{vol} + q\delta\epsilon_{dev}$, where ϕ is the dissipation rate (or increment), and noting that nearly all of the strain increments in, above, and below bands are volume-free at maximum axial sample strain (Figs. 2 *B*, *E*, and *H* and 6 *A*, *D*, and *G*), we conclude that the reported work rates are due almost entirely to deviatoric or frictional processes. Unlike theories in which regions outside of shear bands are dead zones (e.g., ref. 33), as might be suggested in critical state theory as well as by the tendency of dilatancy towards zero in Fig. 6 *A*, *D*, and *G*, regions outside of shear bands clearly continue to store and possibly dissipate (if the assumption of negligible elastic strain is accepted) energy due deviatoric strain and frictional work.

Stress Fluctuations. For particles with 3DXRD measurements of stress at sequential steps of axial sample strain, stress changes were quantified by first computing the stress difference for each particle, p, between these sequential steps and then by computing the SD of these differences for all particles in specific regions, $\mathrm{std}(\sigma^{p,t} - \sigma^{p,t-1})$, where "std" represents the SD, σ is σ_{zz} or q, p is a particle index, t represents a load step, and $t - 1$ represents the prior load step. These SDs are shown for all particles in, above, and below shear bands in Fig. 6 *C*, *F*, and *I* for samples subjected to 20, 30, and 35 MPa, respectively. Although one may expect stress fluctuations to reflect increases in average sample stress during strain increments featuring macroscopic hardening (i.e., when macroscopic stress is increasing), stress fluctuations do not decay to zero at large strains when both axial and deviatoric stresses plateau. Instead, stress fluctuations remain nearly constant at all sample strains and for all sample confining pressures both in and out of shear bands. The stress fluctuations at these large sample strains are also significantly larger than the resolution of 3DXRD stress measurements mentioned earlier (12 and 6 MPa for on- and off-diagonal stress tensor components, respectively), confirming that the fluctuations are not the result of noisy measurements. This finding suggests that there is significant activity of either elastic or plastic work continuing both in and out of shear bands even at maximum axial sample strain, challenging the notion that regions outside of shear bands can be treated as dead zones (33).

Conclusions

In this study, we made in situ grain stress and local strain measurements in triaxially compressed sand samples using XRCT and 3DXRD. XRCT and 3DXRD measurements revealed the evolution of stresses and strains within or around individual grains as well as in and out of shear bands. Samples were subjected to between 20 and 35 MPa confining pressures and featured very little volumetric strain at the largest axial sample strains. Our major findings are summarized as follows:

1) Shear bands identified by fitting a plane through regions of enhanced axial sample compaction or deviatoric strain featured significant deviatoric strains and grain rotations. Such regions also featured significantly elevated deviatoric stresses and deviatoric to mean stress ratios relative to regions outside of shear bands and to the total sample. This suggests that macroscopic measurements of stress in triaxial tests do not necessarily reflect the stress states within specific regions in the sample, motivating careful interpretation of triaxial tests and construction of constitutive laws accounting for these differences (55).
2) Although volumetric strain was slightly compactive within shear bands and nearly constant-volume outside of bands, as expected at the high confining pressures featured here (2, 13), all regions continued to sustain nonnegligible deviatoric strains, work rates, and stress fluctuations throughout the entirety of experiments. Although samples approached a state of minimal dilatancy and constant deviatoric to mean stress ratio at maximum sample strains, elastic or plastic activity continued to occur outside of shear bands with no indication that "dead zones" were formed in contrast to prior assumptions (33).
3) Shear bands featured significant axial contraction along the shear direction in contradiction to zero-extension assumptions made by Roscoe and others (29) but consistent with prior experimental observations (e.g., refs. 13 and 41).
4) Principal compressive stress and both principal compressive strain rates and globally imposed strain rates were remarkably well-aligned throughout all experiments both in and out of shear bands, suggesting minimal stress and strain rate rotations in and out of shear bands.

While the triaxial tests described here were performed using small samples and high confining pressures relevant to rock mechanics and geologic reservoirs, this research nevertheless provides some of the first in situ data with which to assess common postulates of continuum plasticity theories used for modeling soils and rocks.

Materials and Methods

Sample Assembly and Testing. Data were obtained at the ID-1-E beamline of APS. The triaxial compression instrument used in the experiments is shown in Fig. 1*A* and is described in detail in ref. 67 and was used in a previous study on triaxial compression of Ottawa sand (13). Samples of single-crystal alpha-quartz were manufactured from blocks of hydrothermally grown SiO_2 provided by Sawyer Technical Materials, LLC. The blocks were first chiseled and ball-milled and subsequently air-milled in a custom-built air mill at 20 psi as described in ref. 80. Finally, grains were sieved to retain those with approximate diameters between 150 μm and 212 μm. The grain size distribution and characteristics are described in *SI Appendix*, but we note here that grains are well rounded with a median grain size $D_{50} = 125$ μm and sphericity generally between 0.7 and 1, comparable to the sizes and morphologies of the natural Ottawa sand sample with a D_{50} of approximately 175 μm described in ref. 13.

To prepare samples in the triaxial compression instrument, a membrane of about 1.4 mm inner diameter and 3 mm outer diameter was first made using an aluminum mold and AS40 Addition Cure Silicon Rubber from Easy Composites Ltd. The membrane was then placed around a 10-mm pin mounted on the lower shaft of the triaxial compression instrument shown in the *Inset* to figure 1*A* and in ref. 67. Grains were poured into the membrane to a desired height and a top pin with a diameter of 1.58 mm (tool steel ejector pin, part 93772A103 from McMaster-Carr) was inserted into the top of the membrane. Above the 1.58-mm solid pin inserted into the top of the membrane was a 6.35-mm diameter cap to the tool steel ejector pin. Vacuum grease was applied to the exterior of the membrane where it contacted the bottom pin and top ejector pin to prevent fluid from entering the sample environment. The triaxial compression apparatus was then assembled as described in ref. 67 and a top shaft with a 3.125 mm radius hemispherical tip was brought into contact with the cap of the ejector pin. The fluid in the Al tube shown in Fig. 1*A* was then pressurized to the desired confining pressure and the experiment proceeded by quasistatically imposing small axial strain increments to samples, between which axial sample strain was paused for XRCT and 3DXRD measurements.

Downloaded from https://www.pnas.org by "JOHN HOPKINS UNIVERSITY, MT WASHINGTON SHERIDAN LIB TECH SERVICES" on August 9, 2023 from IP address 162.129.251.86.

The confining pressure obtained by averaging grain stresses measured through 3DXRD (reported Fig. 1*D*) was lower than that imposed on the samples even though there were no pressure drops visible on the analog pressure gauge (Fig. 1*A*) after each increment of sample axial strain, with the exception of the 1.4 MPa pressure drop observed during the last strain increment of the sample subjected to 20 MPa (described in the main text). Each sample's measured mean stress may have deviated from the imposed confining pressures at the beginning of the experiments for several reasons. The presence of a membrane around samples is one possible reason, but as described more in the *SI Appendix*, the membrane stiffness alone is unlikely to explain the magnitude of the discrepancy.

Data Acquisition and Analysis. While axial sample strains were held constant, samples were rotated for XRCT and 3DXRD measurements. Because of the limitations of beam heights for imaging (1 mm) and diffraction (0.6 mm), XRCT scans were performed in four layers within each sample with 0.1 mm overlap between layers and 3DXRD scans were performed at seven layers with 0.15 mm overlap between layers. The beam energy for all measurements was 71.676 keV. For XRCT scans of each layer, 2,800 radiographs were obtained on a Retiga 4000DC camera at equal rotation increments during 360° rotation of the sample. For 3DXRD scans of each layer, 3,600 2D diffraction patterns were obtained at equal rotation increments during 360° rotation of the sample on a GE-41RT area detector positioned about 1.53 m downstream of the sample along the X-ray path.

Tomography Data Analysis for Kinematics and Local Strain. Tomography images were reconstructed in TomoPy (71) using the ASTRA toolbox and the SIRT reconstruction algorithm (81). Tomographic images featured a resolution of 1.172 μm/pixel. After the generation of tomographic images for all four layers of each load step for a given sample, the tomographic images were merged by first performing rigid-body digital volume correlation (DVC) on the overlapping region between layers and then translating and rotating one of the layers according to the results (72). This merging process continued until tomographic images were generated for the entire sample. Each sequential pair of full-height XRCT reconstructions for each sample were registered in SPAM to yield an incremental deformation gradient, $\delta \boldsymbol{F}$, and rigid body translation and rotation between images (72). The incremental deformation gradient $\delta \boldsymbol{F}$ was used to compute the axial sample strain presented in all figures in the main text by $\delta\epsilon \approx 1 - \delta F_{zz}$.

The full reconstructed image for the first load step of each experiment was first binarized to separate voids and grains using Otsu's method in Matlab®. Grains were then segmented and assigned unique greyscale values by watershed segmentation, connected components, and region properties functions within Matlab®. Using XRCT reconstructions from the first and second scan of each experiment, along with the segmented image of the first scan, we performed discrete DVC using the volume of each grain as a correlation volume. Through this DVC approach, each grain was assigned an incremental displacement and rotation (the latter reported in Fig. 2), as well as an incremental deformation gradient which was very close to the identity.

To compute the local strain in the voids around each grain, we first constructed a Voronoi tessellation using voro++ (82). We constructed the dual map of this tessellation, a Delaunay triangulation, in Matlab®(73). We then used particle displacements obtained from discrete DVC and adopted the formula in ref. 73, as used in prior work (40), to compute the displacement gradient in each tetrahedron of the triangulation by

$$u^t_{i,j} = \frac{1}{V^t} \sum_{k=1}^{4} u^k_i a^k_i, \quad [1]$$

where V^t is the tetrahedron volume from the Delaunay triangulation, u^k_i is the displacement of grain k forming one of the four nodes of the tetrahedron, and a^k_i is the area vector of the face of the tetrahedron not containing grain k (73). The incremental small strain tensor for each tetrahedron t was then computed by $\delta\epsilon^t_{ij} = 1/2(u^t_{i,j} + u^t_{j,i})$. The local incremental strain for each grain was obtained by volume-averaging tetrahedron strains for all tetrahedrons for which the grain was a node. Incremental strains were subsequently homogenized in regions for some computations by computing an average of local incremental strains weighted by Voronoi volumes obtained from voro++.

3DXRD Analysis for Grain Stress. 3DXRD analysis was performed in MIDAS (83). Five diffraction rings of quartz that did not overlap with rings generated by the Al tube were chosen for analysis (they are identified in Fig. 1*B*). Lattice constants $a = b = 4.917$, $c = 5.407$, $\alpha = \beta = 90°$, $\gamma = 120°$ were used, which provided a mean grain stress consistent with the applied mean grain stress in each experiment and a grain completeness exceeding 80%, a metric often used to ensure accurate position, orientation, and strain fits for each grain (84, 85). Based on prior work with these grains (68, 69), we estimate that the fitting process generated grain strain tensors with 10^{-4} resolution for on-diagonal and 5×10^{-5} for off-diagonal tensor components. This corresponds to grain stress resolution of about 12 MPa and 6 MPa for on- and off-diagonal stress tensor components, respectively. More detail regarding the total number of XRCT grains and successfully fit with grain stresses is provided in *SI Appendix*.

Homogenized Stress. Stresses were homogenized in regions or throughout the entire sample by $\boldsymbol{\sigma} = \phi_s(1/N_g)\sum_g \boldsymbol{\sigma}^g$, where ϕ_s is the solid fraction, N_g is the number of grains in a region, and $\boldsymbol{\sigma}^g$ is the grain stress tensor obtained from 3DXRD. This is akin to calculating the volume-averaged stress across N_g grains by (73)

$$\boldsymbol{\sigma} = \frac{1}{V_t} \sum_{p=1}^{N_g} V_p \boldsymbol{\sigma}^p, \quad [2]$$

where V_p is the particle volume, $\boldsymbol{\sigma}^p$ is the particle stress tensor, and V_t is the total volume in the homogenization volume (i.e., ϕ_s accounts for normalization by V_t rather than the sum of V_p across the corresponding grains).

Data, Materials, and Software Availability. All data are described in *SI Appendix* or can be accessed through www.zenodo.org, as described in *SI Appendix*. X-ray tomography images and diffraction data have been deposited in Zenodo (https://zenodo.org/record/7582286) (86).

ACKNOWLEDGMENTS. We acknowledge the support from the U.S. NSF CAREER Award No. CBET-1942096. Experiments were performed under General User Proposal-72658 at the Advanced Photon Source (APS) beamline ID-1. We are grateful for this beamtime and assistance from beamline scientists Peter Kenesei and Jun-Sang Park. Use of APS, an Office of Science User Facility operated for the U.S. Department of Energy (DOE) Office of Science by Argonne National Laboratory, was supported by the U.S. DOE under Contract No. DE-AC02-06CH11357.

1. A. N. Schofield, P. Wroth, *Critical State Soil Mechanics* (McGraw-Hill, London, UK, 1968), vol. 310.
2. T.-F. Wong, P. Baud, The brittle–ductile transition in porous rock: A review. *J. Struct. Geol.* **44**, 25–53 (2012).
3. S. J. Poulos, The steady state of deformation. *J. Geotech. Eng. Div.* **107**, 553–562 (1981).
4. K. Been, M. G. Jefferies, A state parameter for sands. *Géotechnique* **35**, 99–112 (1985).
5. X. S. Li, Y. F. Dafalias, Anisotropic critical state theory: Role of fabric. *J. Eng. Mech.* **138**, 263–275 (2012).
6. M. Coop, K. Sorensen, T. Bodas Freitas, G. Georgoutsos, Particle breakage during shearing of a carbonate sand. *Géotechnique* **54**, 157–163 (2004).
7. Z. Gao, J. Zhao, X. S. Li, Y. F. Dafalias, A critical state sand plasticity model accounting for fabric evolution. *Int. J. Numer. Anal. Methods Geomech.* **38**, 370–390 (2014).
8. Y. F. Dafalias, Must critical state theory be revisited to include fabric effects? *Acta Geotech.* **11**, 479–491 (2016).
9. L. Luzzani, C. MR, On the relationship between particle breakage and the critical state of sands. *Soils Found.* **42**, 71–82 (2002).
10. A. W. Bishop, D. J. Henkel, *The Measurement of Soil Properties in the Triaxial Test* (Edward Arnold Publishers, London, UK, 1970).
11. M. Coop, I. Lee, "The behaviour of granular soils at elevated stresses" in *Predictive Soil Mechanics: Proceedings of the Wroth Memorial Symposium held at St Catherine's College* (Thomas Telford Publishing, 1992), pp. 186–198.
12. R. Alikarami, E. Andò, M. Gkiousas-Kapnisis, A. Torabi, G. Viggiani, Strain localisation and grain breakage in sand under shearing at high mean stress: Insights from in situ X-ray tomography. *Acta Geotech.* **10**, 15–30 (2015).

Downloaded from https://www.pnas.org by "JOHN HOPKINS UNIVERSITY, MT WASHINGTON SHERIDAN LIB TECH SERVICES" on August 9, 2023 from IP address 162.129.251.86.

13. G. Shahin, R. C. Hurley, Micromechanics and strain localization in sand in the ductile regime. *J. Geophys. Res.: Solid Earth* **127**, e2022JB024983 (2022).
14. T. Liu *et al*., The behaviour of a low-to medium-density chalk under a wide range of pressure conditions. *Soils Found.* **63**, 101268 (2023).
15. P. Bésuelle, J. W. Rudnicki, Localization: Shear bands and compaction bands. *Int. Geophys. Ser.* **89**, 219–322 (2004).
16. G. C. Rawling, L. B. Goodwin, Cataclasis and particulate flow in faulted, poorly lithified sediments. *J. Struct. Geol.* **25**, 317–331 (2003).
17. G. C. Rawling, L. B. Goodwin, Structural record of the mechanical evolution of mixed zones in faulted poorly lithified sediments, Rio Grande Rift, New Mexico, USA. *J. Struct. Geol.* **28**, 1623–1639 (2006).
18. E. Skurtveit, A. Torabi, R. H. Gabrielsen, M. D. Zoback, Experimental investigation of deformation mechanisms during shear-enhanced compaction in poorly lithified sandstone and sand. *J. Geophys. Res.: Solid Earth* **118**, 4083–4100 (2013).
19. E. Skurtveit *et al*., Sand textural control on shear-enhanced compaction band development in poorly-lithified sandstone. *J. Geol. Res. Eng.* **2**, 115–130 (2014).
20. S. J. Hangx, N. Brantut, Micromechanics of high-pressure compaction in granular quartz aggregates. *J. Geophys. Res.: Solid Earth* **124**, 6560–6580 (2019).
21. C. Marone, C. Scholz, Particle-size distribution and microstructures within simulated fault gouge. *J. Struct. Geol.* **11**, 799–814 (1989).
22. F. Balsamo, L. Aldega, N. De Paola, I. Faoro, F. Storti, The signature and mechanics of earthquake ruptures along shallow creeping faults in poorly lithified sediments. *Geology* **42**, 435–438 (2014).
23. J. W. Rudnicki, J. Rice, Conditions for the localization of deformation in pressure-sensitive dilatant materials. *J. Mech. Phys. Solids* **23**, 371–394 (1975).
24. I. Vardoulakis, Shear band inclination and shear modulus of sand in biaxial tests. *Int. J. Numer. Anal. Methods Geomech.* **4**, 103–119 (1980).
25. I. Vardoulakis, M. Goldscheider, G. Gudehus, Formation of shear bands in sand bodies as a bifurcation problem. *Int. J. Numer. Anal. Methods Geomech.* **2**, 99–128 (1978).
26. G. Buscarnera, R. T. Laverack, Path dependence of the potential for compaction banding: Theoretical predictions based on a plasticity model for porous rocks. *J. Geophys. Res.: Solid Earth* **119**, 1882–1903 (2014).
27. A. Drescher, G. Jong, "Photoelastic verification of a mechanical model for the flow of a granular material" in *Journal of the Mechanics and Physics of Solids* (Springer, 1972), vol. 20, pp. 337–351.
28. M. R. Kuhn, *Granular Geomechanics* (Elsevier, 2017).
29. K. H. Roscoe, The influence of strains in soil mechanics. *Geotechnique* **20**, 129–170 (1970).
30. P. W. Rowe, L. Barden, Importance of free ends in triaxial testing. *J. Soil Mech. Found. Div.* **90**, 1–27 (1964).
31. J. Arthur, T. Dunstan, Q. Al-Ani, A. Assadi, Plastic deformation and failure in granular media. *Geotechnique* **27**, 53–74 (1977).
32. M. Bolton, The strength and dilatancy of sands. *Geotechnique* **36**, 65–78 (1986).
33. A. Tordesillas, S. Zhou, J. Bailey, H. Bondell, A representation learning framework for detection and characterization of dead versus strain localization zones from pre-to post-failure. *Granular Matter* **24**, 1–19 (2022).
34. M. Oda, J. Konishi, Microscopic deformation mechanism of granular material in simple shear. *Soils Found.* **14**, 25–38 (1974).
35. M. Oda, J. Konishi, S. Nemat-Nasser, Experimental micromechanical evaluation of strength of granular materials: Effects of particle rolling. *Mech. Mater.* **1**, 269–283 (1982).
36. M. Oda, T. Takemura, M. Takahashi, Microstructure in shear band observed by microfocus X-ray computed tomography. *Géotechnique* **54**, 539–542 (2004).
37. S. A. Hall *et al*., Discrete and continuum analysis of localised deformation in sand using X-ray μct and volumetric digital image correlation. *Geotechnique* **60**, 315–322 (2010).
38. E. Andò, S. A. Hall, G. Viggiani, J. Desrues, P. Bésuelle, Grain-scale experimental investigation of localised deformation in sand: A discrete particle tracking approach. *Acta Geotech.* **7**, 1–13 (2012).
39. J. Desrues, R. Chambon, M. Mokni, F. Mazerolle, Void ratio evolution inside shear bands in triaxial sand specimens studied by computed tomography. *Geotechnique* **46**, 529–546 (1996).
40. C. Zhai, E. Herbold, S. A. Hall, R. C. Hurley, Particle rotations and energy dissipation during mechanical compression of granular materials. *J. Mech. Phys. Solids* **129**, 19–38 (2019).
41. A. Rechenmacher, S. Abedi, O. Chupin, Evolution of force chains in shear bands in sands. *Geotechnique* **60**, 343–351 (2010).
42. A. L. Rechenmacher, S. Abedi, O. Chupin, A. D. Orlando, Characterization of mesoscale instabilities in localized granular shear using digital image correlation. *Acta Geotech.* **6**, 205–217 (2011).
43. C. Chang, T. Matsushima, X. Lee, Heterogeneous strain and bonded granular structure change in triaxial specimen studied by computer tomography. *J. Eng. Mech.* **129**, 1295–1307 (2003).
44. A. Tordesillas, S. Pucilowski, Q. Lin, J. F. Peters, R. P. Behringer, Granular vortices: Identification, characterization and conditions for the localization of deformation. *J. Mech. Phys. Solids* **90**, 215–241 (2016).
45. I. Einav, Breakage mechanics–Part I: Theory. *J. Mech. Phys. Solids* **55**, 1274–1297 (2007).
46. A. Tengattini *et al*., A thermomechanical constitutive model for cemented granular materials with quantifiable internal variables. Part I–Theory. *J. Mech. Phys. Solids* **70**, 281–296 (2014).
47. R. Kawamoto, E. Andò, G. Viggiani, J. E. Andrade, All you need is shape: Predicting shear banding in sand with LS-DEM. *J. Mech. Phys. Solids* **111**, 375–392 (2018).
48. L. Li, E. Marteau, J. E. Andrade, Capturing the inter-particle force distribution in granular material using LS-DEM. *Granular Matter* **21**, 1–16 (2019).
49. H. P. Jostad, H. Khoa, K. Karapiperis, J. E. Andrade, "Can LS-DEM be used to simulate cyclic behavior of sand?" in *Challenges and Innovations in Geomechanics: Proceedings of the 16th International Conference of IACMAG* (Springer, 2021), vol. 116, pp. 228–235.
50. S. Amirrahmat, A. M. Druckrey, K. A. Alshibli, R. I. Al-Raoush, Micro shear bands: Precursor for strain localization in sheared granular materials. *J. Geotech. Geoenviron. Eng.* **145**, 04018104 (2019).
51. D. Lu *et al*., A method for characterizing the deformation localization in granular materials using the relative particle motion. *Comput. Geotech.* **156**, 105262 (2023).
52. A. Druckrey, K. Alshibli, R. Al-Raoush, Discrete particle translation gradient concept to expose strain localisation in sheared granular materials using 3D experimental kinematic measurements. *Géotechnique* **68**, 162–170 (2018).
53. S. Fazekas, J. Török, J. Kertész, D. E. Wolf, Morphologies of three-dimensional shear bands in granular media. *Phys. Rev. E* **74**, 031303 (2006).
54. M. Wiebicke, E. Andò, G. Viggiani, I. Herle, Measuring the evolution of contact fabric in shear bands with X-ray tomography. *Acta Geotech.* **15**, 79–93 (2020).
55. L. A. Le, G. D. Nguyen, H. H. Bui, J. E. Andrade, Localised failure of geomaterials: How to extract localisation band behaviour from macro test data. *Géotechnique* **72**, 596–609 (2022).
56. G. D. Nguyen, H. H. Bui, A thermodynamics- and mechanism-based framework for constitutive models with evolving thickness of localisation band. *Int. J. Solids Struct.* **187**, 100–120 (2020).
57. S. Schmidt, M. Wiebicke, I. Herle, On the determination and evolution of fabric in representative elementary volumes for a sand specimen in triaxial compression. *Granular Matter* **24**, 97 (2022).
58. R. C. Hurley, S. A. Hall, J. E. Andrade, J. Wright, Quantifying interparticle forces and heterogeneity in 3D granular materials. *Phys. Rev. Lett.* **117**, 098005 (2016).
59. R. C. Hurley, S. A. Hall, J. Wright, Multi-scale mechanics of granular solids from grain-resolved X-ray measurements. *Proc. R. Soc. A: Math. Phys. Eng. Sci.* **473**, 20170491 (2017).
60. M. B. Cil, K. A. Alshibli, P. Kenesei, 3D experimental measurement of lattice strain and fracture behavior of sand particles using synchrotron X-ray diffraction and tomography. *J. Geotech. Geoenviron. Eng.* **143**, 04017048 (2017).
61. W. H. Imseeh, K. A. Alshibli, A. Moslehy, P. Kenesei, H. Sharma, Influence of crystal structure on constitutive anisotropy of silica sand at particle-scale. *Comput. Geotech.* **126**, 103718 (2020).
62. E. Salvatore, G. Modoni, E. Andò, M. Albano, G. Viggiani, Determination of the critical state of granular materials with triaxial tests. *Soils Found.* **57**, 733–744 (2017).
63. T. Qu, Y. Feng, Y. Wang, M. Wang, Discrete element modelling of flexible membrane boundaries for triaxial tests. *Comput. Geotech.* **115**, 103154 (2019).
64. M. Mozaffari, W. Liu, M. Ghafghazi, Influence of specimen nonuniformity and end restraint conditions on drained triaxial compression test results in sand. *Can. Geotech. J.* **59**, 1414–1426 (2022).
65. D. Sheng, B. Westerberg, H. Mattsson, K. Axelsson, Effects of end restraint and strain rate in triaxial tests. *Comput. Geotech.* **21**, 163–182 (1997).
66. E. Peri, L. B. Ibsen, B. V. N. Nielsen, "Influence of sample slenderness and boundary conditions in triaxial test–A review" in *7th International Symposium on Deformation Characteristics of Geomaterials, IS-Glasgow 2019* (EDP Sciences, 2019), p. 02009.
67. G. Shahin, R. C. Hurley, HP-TACO: A high-pressure triaxial compression apparatus for in situ X-ray measurements in geomaterials. *Rev. Sci. Inst.* **93**, 113907 (2022).
68. R. C. Hurley, E. B. Herbold, D. C. Pagan, Characterization of the crystal structure, kinematics, stresses and rotations in angular granular quartz during compaction. *J. Appl. Crystallogr.* **51**, 1021–1034 (2018).
69. R. C. Hurley, Stress and force measurement uncertainties in 3D granular materials in EPJ Web of Conferences. *EDP Sci.* **249**, 02009 (2021).
70. S. G. Kwak, J. H. Kim, Central limit theorem: The cornerstone of modern statistics. *Korean J. Anesthesiol.* **70**, 144–156 (2017).
71. D. Gürsoy, F. De Carlo, X. Xiao, C. Jacobsen, TomoPy: A framework for the analysis of synchrotron tomographic data. *J. Synchrotron Radiat.* **21**, 1188–1193 (2014).
72. O. Stamati *et al*., SPAM: Software for practical analysis of materials. *J. Open Source Software* **5**, 2286 (2020).
73. K. Bagi, Stress and strain in granular assemblies. *Mech. Mater.* **22**, 165–177 (1996).
74. J. Desrues, G. Viggiani, Strain localization in sand: An overview of the experimental results obtained in Grenoble using stereophotogrammetry. *Int. J. Numer. Anal. Methods Geomech.* **28**, 279–321 (2004).
75. A. Saada, L. Liang, J. Figueroa, C. Cope, Bifurcation and shear band propagation in sands. *Geotechnique* **49**, 367–385 (1999).
76. G. Shahin, "Geomechanical modeling of inception and propagation of compaction bands in porous rocks," PhD thesis, Northwestern University (2020).
77. R. Nova, D. M. Wood, A constitutive model for sand in triaxial compression. *Int. J. Numer. Anal. Methods Geomech.* **3**, 255–278 (1979).
78. I. Collins, B. Muhunthan, On the relationship between stress-dilatancy, anisotropy, and plastic dissipation for granular materials. *Geotechnique* **53**, 611–618 (2003).
79. D. W. Taylor, *Fundamentals of Soil Mechanics* (LWW, 1948), vol. 66.
80. M. M. Thakur *et al*., On mesoscale modeling of concrete: Role of heterogeneities on local stresses, strains, and representative volume element. *Cem. Concr. Res.* **163**, 107031 (2023).
81. D. M. Pelt *et al*., Integration of TomoPy and the ASTRA toolbox for advanced processing and reconstruction of tomographic synchrotron data. *J. Synchrotron Radiat.* **23**, 842–849 (2016).
82. C. Rycroft, "Voro++: A three-dimensional voronoi cell library in C++" (Tech. Rep., Lawrence Berkeley National Lab (LBNL), Berkeley, CA, 2009).
83. H. Sharma, R. M. Huizenga, S. E. Offerman, A fast methodology to determine the characteristics of thousands of grains using three-dimensional X-ray diffraction. II. Volume, centre-of-mass position, crystallographic orientation and strain state of grains. *J. Appl. Crystallogr.* **45**, 705–718 (2012).
84. J. Oddershede *et al*., Determining grain resolved stresses in polycrystalline materials using three-dimensional X-ray diffraction. *J. Appl. Crystallogr.* **43**, 539–549 (2010).
85. J. V. Bernier, N. R. Barton, U. Lienert, M. P. Miller, Far-field high-energy diffraction microscopy: A tool for intergranular orientation and strain analysis. *J. Strain Anal. Eng. Design* **46**, 527–547 (2011).
86. R. C. Hurley, G. Shahin, B. S. Kuwik, K. Lee, Dataset for article titled "Assessing continuum plasticity postulates with grain stress and local strain measurements in triaxially compressed sand". Zenodo. https://zenodo.org/record/7582286. Deposited 30 January 2023.

Downloaded from https://www.pnas.org by "JOHN HOPKINS UNIVERSITY, MT WASHINGTON SHERIDAN LIB TECH SERVICES" on August 9, 2023 from IP address 162.129.251.86.